Journal of Colloid and Interface Science 555 (2019) 449–459

Contents lists available at ScienceDirect

Journal of Colloid and Interface Science

journal homepage: www.elsevier.com/locate/jcis

Regular Article

Facile design of ultrafine Co_7Fe_3 nanoparticles coupled with nitrogen-doped porous carbon nanosheets for non-enzymatic glucose detection

Mian Li [a,*], Jirong Yang [a], Mingjiao Lu [a], Yingjie Zhang [a,*], Xiangjie Bo [b,*]

[a] National and Local Joint Engineering Laboratory for Lithium-ion Batteries and Materials Preparation Technology, Key Laboratory of Advanced Battery Materials of Yunnan Province, Faculty of Metallurgical and Energy Engineering, Kunming University of Science and Technology, Kunming 650093, China

[b] Key Laboratory of Nanobiosensing and Nanobioanalysis at Universities of Jilin Province, Department of Chemistry, Northeast Normal University, Changchun, Jilin Province 130024, China

GRAPHICAL ABSTRACT

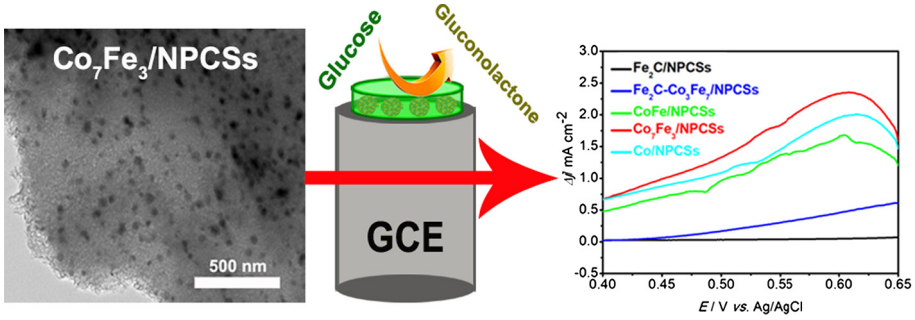

ARTICLE INFO

Article history:
Received 16 April 2019
Revised 29 July 2019
Accepted 30 July 2019
Available online 31 July 2019

Keywords:
Biomass
Porous carbon nanosheets
Co_7Fe_3 alloy nanoparticles
Non-enzymatic detection
Glucose
Biosensor

ABSTRACT

Ultrafine Co_7Fe_3 nanoparticles embedded in nitrogen-doped porous carbon nanosheets (denoted as Co_7Fe_3/NPCSs) are successfully synthesized by utilizing porous plant tissue as a precursor. The morphological, structural, and chemical contents of the Co_7Fe_3/NPCSs and other control samples are analyzed by X-ray (powder) diffraction (XRD), scanning electron microscopy (SEM), transmission electron microscopy (TEM), N_2 adsorption–desorption, Raman spectroscopy, inductively coupled plasma (ICP), and X-ray photoelectron spectroscopy (XPS) techniques. The glucose oxidation and detection performances of each catalyst are evaluated by using cyclic voltammetry and chronoamperometry. The experimental results demonstrate that the electrocatalytic abilities of the resultant catalysts toward glucose oxidation decrease in the order of Co_7Fe_3/NPCSs > Co/NPCSs > CoFe/NPCSs > Fe_2C-Co_3Fe_7/NPCSs > Fe_2C/NPCSs. The experimental results prove that a small number of Fe atoms in Co_7Fe_3 can increase the number of active Co^{4+} sites. Meanwhile, the ultrafine Co_7Fe_3 nanoparticles uniformly dispersed along the porous carbon nanosheets' surfaces, which further improved the dispersion of the abundant electrochemically available active sites. Due to the synergistic effect of the hierarchical porous structures, high-density active sites and excellent electron conductivity, the optimal Co_7Fe_3/NPCSs display the best glucose detection efficiency of all the catalysts examined. For instance, the Co_7Fe_3/NPCSs exhibit large sensitivity values (795.28 μA cm^{-2} mM^{-1} between 0.001 and 2.20 mM and 401.98 μA cm^{-2} mM^{-1} between 2.20 and 14.00 mM), a rapid response time (2.2 s), a low detection limit (1.0 μM), excellent anti-interference toward electroactive molecules, a perfect reproducibility and a superior long-term stability. The Co_7Fe_3/NPCSs also exhibit a satisfying efficiency for glucose detection in human serum samples.

* Corresponding authors.
E-mail addresses: lim148@kmust.edu.cn (M. Li), zyjkmust@126.com (Y. Zhang), baoxj133@nenu.edu.cn (X. Bo).

https://doi.org/10.1016/j.jcis.2019.07.099

Finally, our low-cost synthetic strategy can advance research used for designing 3D hierarchical meso/macroporous noble-metal-free catalysts without any tedious steps or templates.

1. Introduction

It is well known that more than 300 million patients are suffering from diabetes, which therefore has been identified as one of the most serious health concerns of the 21st century [1]. Medical research has revealed the cause of diabetes, in which an insulin deficiency ascribed to a metabolic disorder of the body results in obvious hyperglycemia. In general, diabetes can be diagnosed by detecting patients' blood glucose concentrations and comparing the test results with the normal glucose concentration ranges of a healthy person (80–120 mg dL^{-1}) [2]. Therefore, developing advanced glucose sensors with high detection performances is extremely pivotal for diagnosing and managing diabetes mellitus. As glucose oxidase (GO_x) can efficiently catalyze the glucose oxidization reaction, Karl Erik Hellström and Ingegerd Hellström have successfully designed the first GO_x-based sensor for glucose concentration detection [3]. Since then, GO_x-based glucose sensors have been extensively studied and improved to exhibit high sensitivities and selectivities. Nevertheless, enzymes are often unstable, and thus, GO_x-based glucose sensors inevitably suffer from worsening long-term stabilities [4].

Based on the existing facts referring to GO_x-based glucose sensors, developing non-enzymatic glucose sensors are therefore becoming increasingly important as an alternative technique [5]. To design non-enzymatic alternatives with outstanding glucose catalytic efficiencies and stabilities, many efforts have been made. For example, noble metal platinum [6], palladium [7], and their alloys [8–10] have been widely utilized for non-enzymatic glucose detection. Nevertheless, the adsorption of intermediate/chloride compounds usually causes damage to the surface and reduces the electrocatalytic activity of noble metals [11]. Meanwhile, most active compounds coexisting in blood (for instance, ascorbic acid (AA), dopamine (DA), uric acid (UA), lactic acid (LA), and glutaric acid (GA)) will cause unavoidable interferences [12]. Finally, the high cost and scarcity of noble metals also limits their commercialization for glucose sensor applications.

To overcome the drawbacks of noble metals and the GO_x enzyme, developing active, stable, and inexpensive glucose sensors based on non-enzymatic compounds is still extremely urgent. Until now, large amounts of compounds based on transition metals (nickel (Ni), copper (Cu), cobalt (Co), etc.) or transition metal oxides (ferroferric oxide (Fe_3O_4), nickel oxide (NiO), copper oxide (CuO), etc.) have been widely researched and utilized for glucose sensors [5,11,13–17]. Among these non-enzymatic glucose sensors, Co-based oxides (CoO_x) are of interest due to their specific morphologies/structures, low-cost, polyvalence characteristics and excellent catalytic activities [18,19]. However, the weak electron conductivity of CoO_x is a significant drawback that prevents it from exhibiting excellent glucose detection properties [12]. Two strategies are usually adopted to promote the electron transport capacities of metal oxides: (1) Perfect electron conductors are introduced, for example, graphitic carbon matrices, as carbon matrices can promote the electron transport efficiencies of CoO_x in electrochemical reactions [20–22]. (2) Metallic particles coupled with graphitic carbon matrices are designed. For this kind of compound, in electrochemical catalysis processes, the outer surfaces of metallic particles transform into active sites with high valence states. For Co@CoO_x core-shell structures coupled with graphitic carbon matrices, in electrochemical catalysis processes, the inner metallic core can enhance the transport of electrons derived from the outer active sites [23,24]. On the other hand, a deficiency of active sites is another drawback that limits the electrocatalytic abilities of metal oxides [25]. Introducing mesoporous carbon matrices with large surface areas and abundant carbon defects can obviously enhance the number of electrochemically available active sites [26,27], This occurs because the abundant mesopores and carbon edges/defects can efficiently prevent the aggregation of active sites [28,29]. Based on the abovementioned facts, small Co nanoparticles embedded in porous carbons may have great potential for the commercialization and industrialization of non-enzymatic glucose sensors.

It is well known that biological tissues containing abundant nutrient transport channels are perfect precursors for constructing porous carbons. A paper towel is made from plant tissues with various porous channels. Herein, by strategically utilizing the porous structures of paper towels, cobalt acetates can uniformly adsorb and disperse in paper towels. After calcining in a nitrogen (N_2) atmosphere at 800 °C, nitrogen-doped meso/macroporous carbon nanosheets embedded with small metallic Co nanoparticles (denoted as Co/NPCSs) were successfully prepared. Several previous reports have revealed that combining a second transition metal element (such as Ni, Fe, or Mn) into Co-based materials is advantageous to improving the electrocatalytic efficiencies of the Co-based material [30–32]. Therefore, to enhance the intrinsic catalytic ability of the Co-based active sites, Fe has been chosen as the doping element. The as-prepared catalysts were characterized by using X-ray diffraction (XRD), scanning electron microscopy (SEM), transmission electron microscopy (TEM), N_2 adsorption-desorption, Raman spectroscopy, inductively coupled plasma-optical emission spectrometry (ICP-OES) and X-ray photoelectron spectroscopy (XPS) techniques. After optimizing the doping amounts of Fe atoms, the optimal Co_7Fe_3/NPCSs material exhibited the best glucose oxidation ability compared with the other control samples (such as Fe_2C-Co_3Fe_7/NPCSs, CoFe/NPCSs, and Co/NPCSs). On the other hand, Co_7Fe_3/NPCSs modified electrodes are appropriate for detecting glucose concentrations in not only standard glucose samples but also real human serum samples.

2. Experimental

2.1. Reagents and apparatus

Glucose, UA, DA, AA, LA, GA, cobalt acetate ($Co(AC)_2{\cdot}4H_2O$), iron acetate ($Fe(AC)_2{\cdot}4H_2O$), cyanamide (CN_2H_2), saccharose ($C_{12}O_{11}H_{22}$), sodium chloride (NaCl) and sodium hydroxide (NaOH) were purchased from Sinopharm Chemical Reagent C. All of these chemical reagents were of analytical grade and used as received. The Fresh Air brand paper towels were purchased from Walmart. Ultrapure water (resistivity: $\rho \geq 18$ MΩ cm^{-1}) was utilized to prepare the solutions.

2.2. Catalyst synthesis

Scheme 1 exhibits the detailed method used to synthesize the Co_7Fe_3/NPCSs. Approximately 30 mL of a solution containing 0.9 mmol $Fe(AC)_2$ and 2.1 mmol $Co(AC)_2$ was prepared and used as the impregnating solution (denoted as $[Fe(AC)_2]_{0.9}$-$[Co(AC)_2]_{2.1}$). Then, 1 g paper towels were impregnated for 24 h in

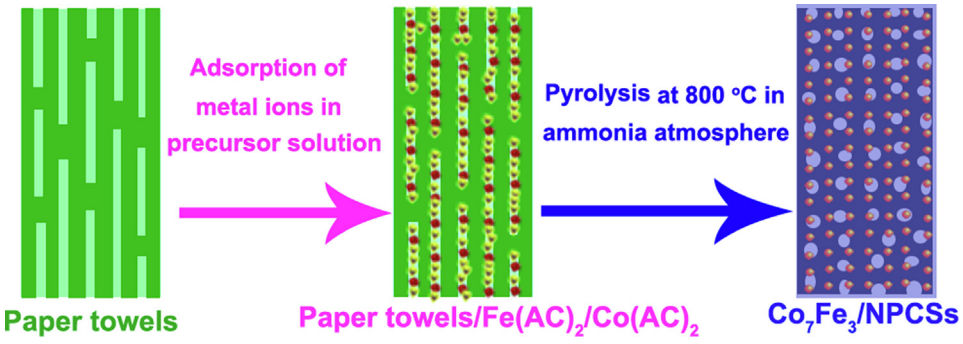

Scheme 1. Procedures used to synthesize the Co_7Fe_3/NPCSs material.

the aforementioned $[Fe(AC)_2]_{0.9}$-$[Co(AC)_2]_{2.1}$ impregnating solution. Closely afterwards, the resultant paper towels-$[Fe(AC)_2]_{0.9}$-$[Co(AC)_2]_{2.1}$ solid substances were dried at 40 °C and pyrolyzed in a N_2 atmosphere for 2 h at 800 °C. For comparison, the Fe_2C/NPCSs, Fe_2C-Co_3Fe_7/NPCSs, CoFe/NPCSs and Co/NPCSs control materials were synthesized by utilizing $Fe(AC)_2]_{3.0}$, $[Fe(AC)_2]_{2.1}$-$[Co(AC)_2]_{0.9}$, $[Fe(AC)_2]_{1.5}$-$[Co(AC)_2]_{1.5}$ and $[Co(AC)_2]_{0.3}$ impregnating solutions, respectively. All the other conditions used to synthesize the Fe_2C/NPCSs, Fe_2C-Co_3Fe_7/NPCSs, CoFe/NPCSs and Co/NPCSs were the same as those used to synthesize the Co_7Fe_3/NPCSs. On the other hand, to determine the critical roles of the porous structures in paper towels for boosting the catalysis efficiency of the Co_7Fe_3/NPCSs, we also prepared another control sample (denoted as Co_7Fe_3/NC) that has few porous structures. The precursor of the Co_7Fe_3/NC is a mixture containing 0.9 mmol $Fe(AC)_2$, 2.1 mmol $Co(AC)_2$, 0.36 mmol CN_2H_2 and 2.9 mmol $C_{12}O_{11}H_{22}$.

2.3. Physical characterization of the resultant materials

The physical characterization techniques used in this paper (such as SEM, XRD, TEM, Raman, N_2 adsorption–desorption, ICP-OES, XPS and energy dispersive X-ray spectroscopy (EDS)) are detailed in the supporting information (*SI*).

2.4. Electrochemical tests

All the working electrodes used in this paper were glassy carbon electrodes (GCE, d = 3 mm) modified by the resultant catalysts. At first, the GCEs were polished by using 1.00, 0.30, and 0.05 μm alumina powders. Afterwards, the polished GCEs were cleaned by using a HNO_3 (1:1) solution, ethanol, and deionized water. Various catalyst inks were prepared by mixing 3 mg catalyst powders in a 1 mL Nafion solution (0.1 wt%). After the ultrasonication treatment, 10 μL as-prepared catalyst inks were then deposited onto the clean GCEs and dried under an infrared lamp. All the electrochemical measurements [cyclic voltammetry (CV) and chronoamperometry (*i-t*)] were performed with a CHI 830B electrochemical workstation (CH Instruments, USA) by using a traditional three-electrode configuration. The catalyst-modified GCEs, Ag/AgCl (in a saturated KCl solution), and platinum wire served as the working, reference, and counter electrodes, respectively. The current density (j) values displayed in this work were recorded as the ratios of the measured current values to the geometric area of the GCE. For the electrochemical tests, all the catalyst-modified GCEs were first analyzed with CV by scanning between 0.0 and +0.65 V *vs.* Ag/AgCl until the CV curves remained unchanged.

3. Results and discussion

3.1. Material characterization

The SEM images of the paper towel recorded at different magnifications are shown in Fig. S1a–c, which reveals giant fiber textures with micron-sized diameters and rough surfaces. The amplifying SEM image further shows that the surfaces of the giant fibers disperse vast corrugated nanosheets (Fig. S1d). The N_2 adsorption–desorption isotherm of the paper towel (Fig. S1e) demonstrates a Brunauer–Emmett–Teller (BET) surface area of 16.39 m^2 g^{-1}. In particular, the pore diameter distribution curve (inset of Fig. S1e) further reveals that the paper towel contains various porous structures with diameters between 2 and 200 nm. The structural characterization results prove the porosity of the paper towel precursor. The elemental mapping analysis of the paper towel precursor is carried out by utilizing EDX (Fig. S2). The elemental mapping image shown in Fig. S2b demonstrates that N- and O-based species are homogeneously distributed along with C atoms. The C (Fig. S2c), O (Fig. S2d), and N (Fig. S2e) concentrations of the paper towel are 53 at.%, 29 at.%, and 4 at.%, respectively. In particular, the O:C ratio is calculated to be ~0.547.

After pyrolyzing in a N_2 atmosphere at 800 °C, the various control samples were successfully synthesized. The XRD patterns (Fig. 1) of the Fe_2C/NPCSs, Fe_2C-Co_3Fe_7/NPCSs, CoFe/NPCSs, Co_7Fe_3/NPCSs, and Co/NPCSs samples all display (0 0 2) diffraction peaks, demonstrating the existence of graphitic carbon. Nevertheless, all the control sample XRD patterns have entirely different diffraction peaks corresponding to metallic phases. For instance, the XRD pattern of the Fe_2C/NPCSs (Fig. 1a) only has characteristic peaks of the pure Fe_2C phase (PDF#36-1249) [33]. Nevertheless, the characteristic peaks of both Fe_2C (PDF#36-1249) and the Co_3Fe_7 alloy (PDF#48-1817) [34] simultaneous appear in the XRD pattern of the Fe_2C-Co_3Fe_7/NPCSs (Fig. 1b). Even so, the peak intensities of Fe_2C are much weaker than those of the Co_3Fe_7 alloy. The XRD patterns of the CoFe/NPCSs (Fig. 1c), Co_7Fe_3/NPCSs (Fig. 1d), and Co/NPCSs (Fig. 1e) have only diffraction peaks corresponding to the pure CoFe alloy (PDF#49-1568) [35], Co_7Fe_3 alloy (PDF#50-0795) [31], and Co (PDF#15-0806) [31], respectively. As seen in Fig. 1b, c, d, the peak positions assigned to Co_7Fe_3 are quite similar to those of Co_3Fe_7 and CoFe. Therefore, we further compared the magnified XRD (1 1 0), (2 0 0) and (2 1 1) peaks of the Co_3Fe_7, CoFe and Co_7Fe_3 alloys in Fig. S3. It is clear that the (1 1 0), (2 0 0) and (2 1 1) peaks in the CoFe alloy XRD pattern occur at much higher diffraction angles than those in the Co_3Fe_7 alloy XRD pattern. Similarly, the (1 1 0), (2 0 0) and (2 1 1) peaks in the Co_7Fe_3 alloy XRD pattern occur at much higher diffraction angles than those in the CoFe alloy XRD pattern. These analysis results demonstrate that the alloy particles dispersed on the different control samples indeed have different chemical compositions.

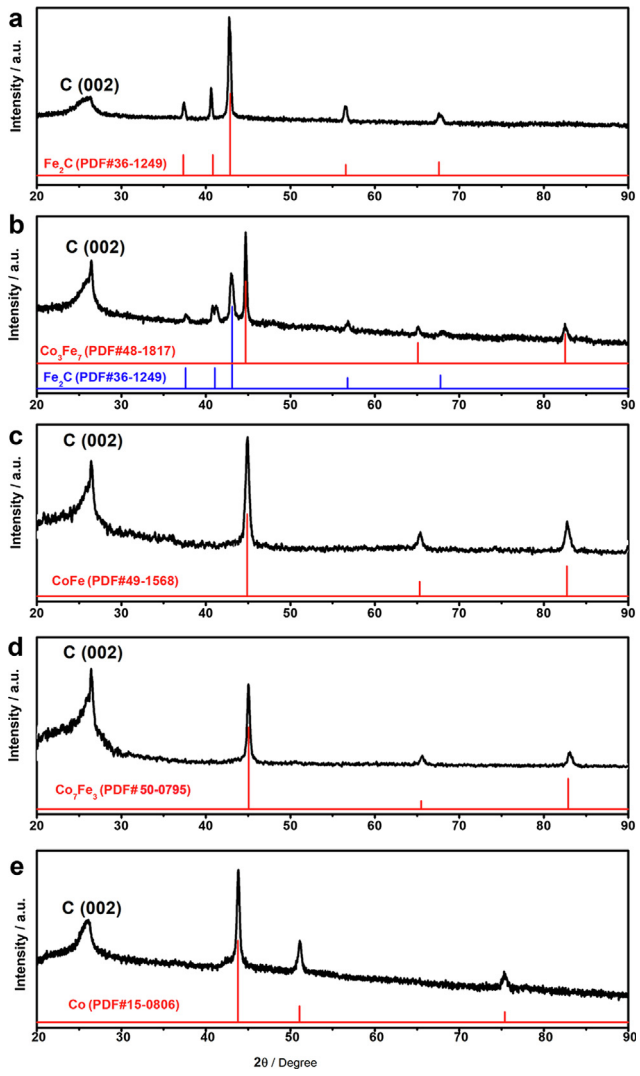

Fig. 1. XRD patterns of the (a) Fe_2C/NPCSs, (b) Fe_2C-Co_3Fe_7/NPCSs, (c) CoFe/NPCSs, (d) Co_7Fe_3/NPCSs, and (e) Co/NPCSs.

The SEM image shows that the Co_7Fe_3/NPCSs consist of large ribbons with diameters larger than 10 μm (Fig. S4a), and the surfaces of the large ribbons are covered by vast corrugated carbon nanosheets. Nevertheless, compared with the precursor ribbons shown in Fig. S1, parts of the giant fibers have decomposed into bulk particles in the pyrolysis processes. The magnified SEM image of the Co_7Fe_3/NPCSs further demonstrates that the vast highly dispersed Co_7Fe_3 nanoparticles with diameters less than 50 nm uniformly dispersed along the surfaces of the corrugated carbon nanosheets (Fig. S4b). To observe the surface structure characteristics of each material in detailed, the TEM images were shown in Fig. 2. Fig. 2 shows that the vast metallic nanoparticles have embedded into the frameworks of the porous carbon nanosheets for all the control samples (Fig. 2a–e). The statistical particle size results reveal that the average particle sizes are 35.18, 33.99, 32.87, 30.71, and 29.97 nm for the Fe_2C/NPCSs (Fig. S5a), Fe_2C-Co_3Fe_7/NPCSs (Fig. S5b), CoFe/NPCSs (Fig. S5c), Co_7Fe_3/NPCSs (Fig. 2f) and Co/NPCSs (Fig. S5d), respectively. The characterization results demonstrate that channels/pores existing in the plant tissues can promote the dispersion of metal salts and restrict the infinite growth of the alloy particles. On the other hand, the particle dispersion is better in the Co_7Fe_3/NPCSs and Co/NPCSs than in the Fe_2C/NPCSs, Fe_2C-Co_3Fe_7/NPCSs and CoFe/NPCSs. The magnified TEM image of the Co_7Fe_3/NPCSs clearly shows that vast mesopores with different diameters have formed along the surfaces of the Co_7Fe_3/NPCSs (Fig. 2g). In addition, Fig. 2h displays the high resolution transmission electron microscopy (HRTEM) image obtained from an individual nanocrystal, and the well-resolved lattice fringes with interplanar spacings of 0.201 nm correspond to the (1 1 0) planes of the Co_7Fe_3 crystal.

The porosities of all the control samples were further characterized by a N_2 adsorption-desorption technique. As shown in Fig. 3a, the N_2 adsorption-desorption isotherms of the five control samples are extremely similar to one another and exhibit characteristics of type IV adsorption isotherms, indicating the wide distribution of porous structures. The specific surface areas calculated from the adsorption data by using the BET method are shown in Fig. 3b, in which all the control samples exhibit similar BET surface areas: 361.9 m^2 g^{-1} for the Fe_2C/NPCSs, 358.3 m^2 g^{-1} for the Fe_2C-Co_3Fe_7/NPCSs, 355.1 m^2 g^{-1} for the CoFe/NPCSs, 347.9 m^2 g^{-1} for the Co_7Fe_3/NPCSs, and 344.5 m^2 g^{-1} the Co/NPCSs. The pore diameter dispersion curves are similar for the five control samples (Fig. 3c). Nevertheless, compared with the pore diameter dispersion curve of the paper towel (shown in the inset of Fig. S1d), more mesopores with diameters smaller than 10 nm appear in all the samples after the pyrolysis processes. Previous reports have proved that these kinds of mesopores are derived from the release of H_2O/CO_2 gases during the carbonation process [31]. Specifically, the amount of mesopores with sizes between 10 and 50 nm for the Fe_2C/NPCSs and Fe_2C-Co_3Fe_7/NPCSs is much larger than that of the CoFe/NPCSs, Co_7Fe_3/NPCSs and Co/NPCSs. This abnormal phenomenon can be attributed to the distribution of metallic nanoparticles on the porous carbon sheets. The HRTEM image (Fig. 2g) proves that the small alloy nanoparticles with diameters between 10 and 50 nm are mainly embedded in the mesopores of the carbon matrices. As shown in Figs. 2 and S5, the CoFe/NPCSs, Co_7Fe_3/NPCSs, and Co/NPCSs contain more alloy nanoparticles (with diameters between 10 and 50 nm) than the Fe_2C/NPCSs and Fe_2C-Co_3Fe_7/NPCSs. Therefore, most of the mesopores (with sizes between 10 and 50 nm) of the CoFe/NPCSs, Co_7Fe_3/NPCSs, and Co/NPCSs are filled with alloy nanoparticles with diameters between 10 and 50 nm, leading to fewer mesopores with sizes between 10 and 50 nm in the pore diameter dispersion curves (Fig. 3c). The Raman spectrum of the Co_7Fe_3/NPCSs (Fig. 3d) shows four broad and overlapping peaks. Among the four peaks, the D (1351 cm^{-1}) and G (1587 cm^{-1}) peaks are fairly sharp, indicating the coexisting graphitic structures and carbon defects. An I_D/I_G value of 1.33 proves the existence of abundant carbon defects/edges.

To further investigate the elemental composition of the Co_7Fe_3/NPCSs catalyst, the Co and Fe contents were detected by an ICP-OES technique (3 replicate experiments were performed). The measurement results show that the mole numbers of Co and Fe atoms in 1 mg Co_7Fe_3/NPCSs are 1.0358×10^{-3} mmol and 2.4067×10^{-3} mmol respectively, demonstrating a Co/Fe molar ratio of 7:3.0127. This molar ratio value is nearly consistent with the 7:3 ratio of the Co_7Fe_3 alloy determined from the XRD pattern of the Co_7Fe_3/NPCSs. To further study the chemical states of the metallic alloy and carbon matrices, XPS was utilized. The XPS survey spectrum confirms the presences of C, O, N, Fe, and Co elements in the Co_7Fe_3/NPCSs (Fig. 4a). Fig. 4b shows the high-resolution C 1s XPS spectrum of the Co_7Fe_3/NPCSs, and the characteristic peaks centered at binding energies of 284.7, 285.6, and 288.4 eV can be assigned to the C—C sp^2, C—N sp^2/C—C sp^3, and C—O groups, respectively. The high resolution O 1 s XPS spectrum of the Co_7Fe_3/NPCSs (Fig. 4c) shows two sharp peaks located at ~532.2 and ~533.8 eV, which are assigned to the oxygen-containing groups dispersed on the material surfaces. In addition, another fairly weak peak located at ~529.8 eV can be observed in the high resolution O 1s XPS

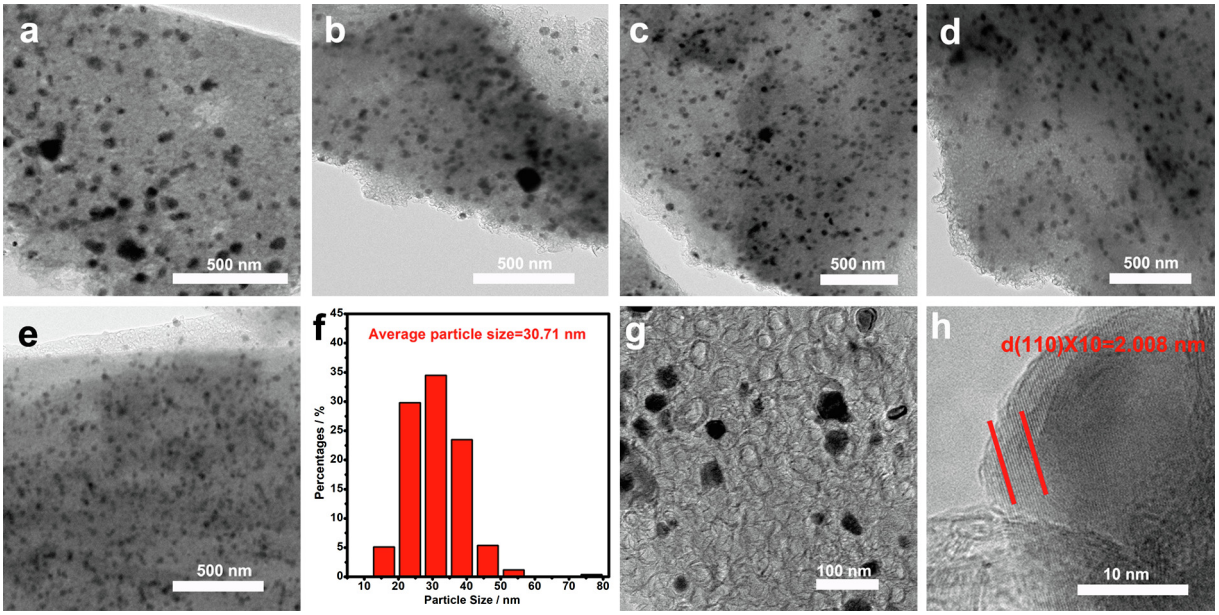

Fig. 2. TEM images of the Fe_2C/NPCSs (a), Fe_2C-Co_3Fe_7/NPCSs (b), CoFe/NPCSs (c), Co_7Fe_3/NPCSs (d) and Co/NPCSs (e). (f) Particle size distribution curve of the Co_7Fe_3/NPCSs. (g, h) HRTEM images of the Co_7Fe_3/NPCSs.

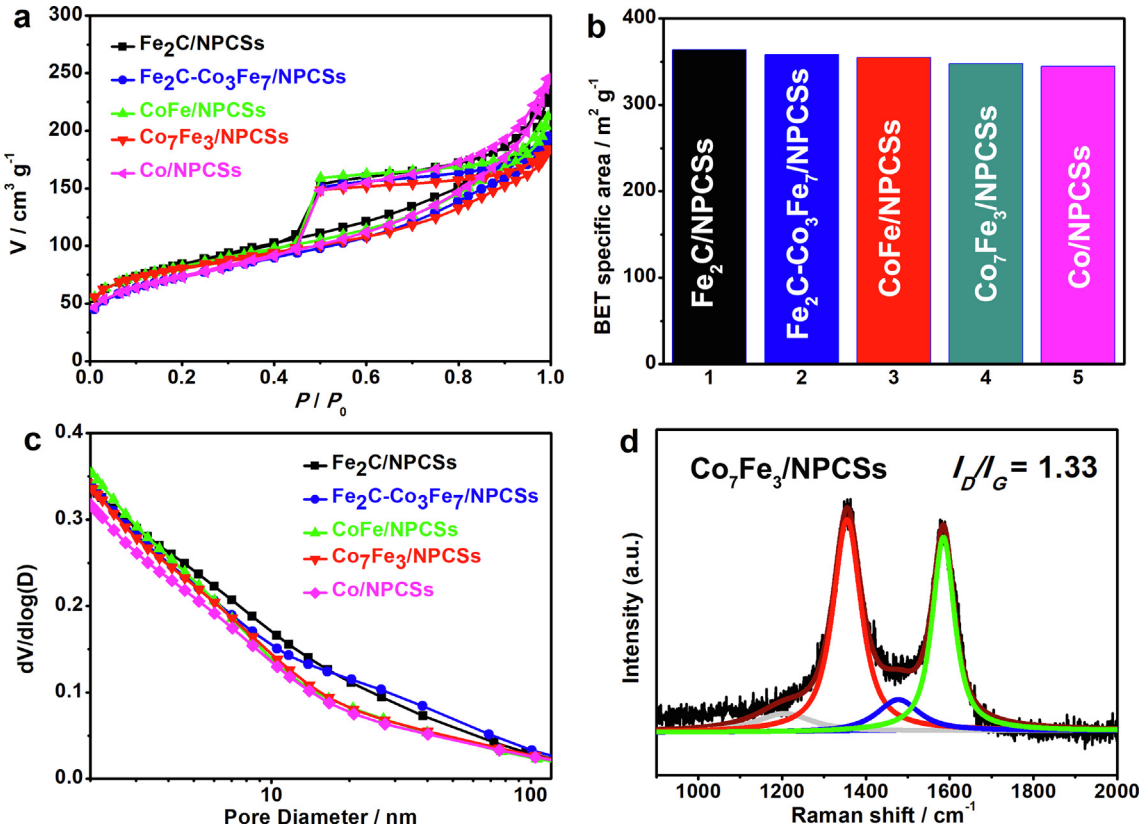

Fig. 3. (a) N_2 adsorption–desorption isotherms, (b) histograms of the BET specific areas and (c) pore diameter distribution curves for the Fe_2C/NPCSs, Fe_2C-Co_3Fe_7/NPCSs, CoFe/NPCSs, Co_7Fe_3/NPCSs and Co/NPCSs control samples. (d) Raman spectrum of the Co_7Fe_3/NPCSs sample.

spectrum of the Co_7Fe_3/NPCSs, which is due to the slight oxidation of the alloy particles on the surfaces. Even so, due to the trace metal oxides, the crystallographic planes were not detected in the XRD pattern (Fig. 1d). As shown in Fig. 4d, the high-resolution N 1s XPS spectrum shows that the N atoms doped into the carbon structures exist in the form of pyridinic N (~398.4 eV), pyrrolic N (~400.7 eV), graphitic N (~402.4 eV), and oxidized N (~406.5 eV), respectively [36]. Finally, to confirm the chemical states of the Co_7Fe_3 alloy nanoparticles, we have fitted the high resolution Co $2p_{3/2}$ (Fig. 4e) and Fe $2p_{3/2}$ (Fig. 4f) XPS spectra of the Co_7Fe_3/NPCSs. It is clear that both the high resolution Co $2p_{3/2}$ (Fig. 4e) and Fe $2p_{3/2}$ (Fig. 4f) XPS spectra exhibit obvious peaks corresponding

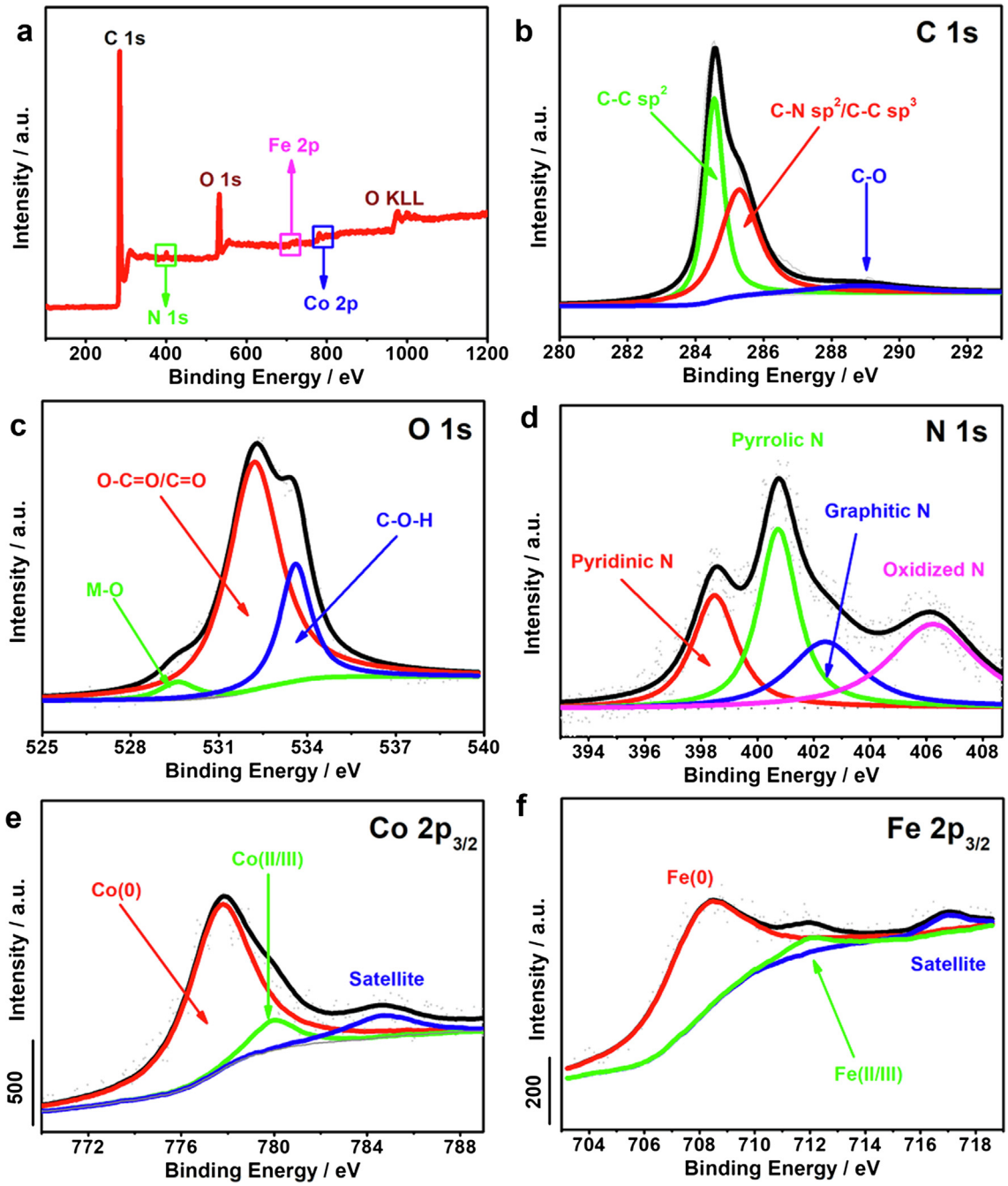

Fig. 4. The XPS survey spectrum (a) and high-resolution XPS spectra of C 1s (b), O 1s (c), N 1s (d), Co 2p (e), and Fe 2p (f) for the Co_7Fe_3/NPCSs.

to metallic Co (~777.9 eV) and metallic Fe (~707.9 eV), demonstrating the successful formation of the Co_7Fe_3 alloy. The weak characteristic peaks of the metal oxides (where the Co oxides correspond to ~ 780.2 eV, and the Fe oxides correspond to ~ 711.5 eV) and satellites appear in the high resolution Co $2p_{3/2}$ and Fe $2p_{3/2}$ XPS spectra, indicating the slight oxidation of the Co_7Fe_3 alloy nanoparticles' surfaces. Nevertheless, the weak characteristic peaks indicate the minor oxidation of the Co_7Fe_3 alloy.

3.2. The electrochemical oxidation of glucose on different catalyst-modified electrodes

A comparative study of the electrocatalytic performance toward glucose oxidation was implemented for the five control catalyst-modified GCEs in a 0.1 M NaOH solution. The CV curves measured in the absence (black lines) and presence (red lines) of 1.0 mM glucose are shown in Fig. 5a–e. No oxidation peaks were present in the CV curves of the Fe_2C/NPCSs/Nafion/GCE (Fig. 5a). By adding a 1 mM glucose solution to the electrolyte, only weak current responses ($\Delta j = j_{\text{with 1.0 mM glucose}} - j_{\text{without glucose}}$) can be found in the selected potential window. The CV curves of the Fe_2C-Co_3Fe_7/NPCSs/Nafion/GCE (Fig. 5b) have distinct different shapes compared with those of the Fe_2C/NPCSs/Nafion/GCE (Fig. 5a). In the absence of the 1.0 mM glucose solution, an obvious redox pair attributed to the irreversible redox processes of Co^{2+}/Co^{3+} appears in the potential region of +0.10 to +0.45 V *vs.* Ag/AgCl for the Fe_2C-Co_3Fe_7/NPCSs/Nafion/GCE. The j values increase for increasing potentials from +0.45 to +0.65 V *vs.* Ag/AgCl in the positive scan, which is mainly attributed to the oxidation of the metal ions from Co^{3+} to Co^{4+}. Furthermore, once the 1.0 mM glucose solution was

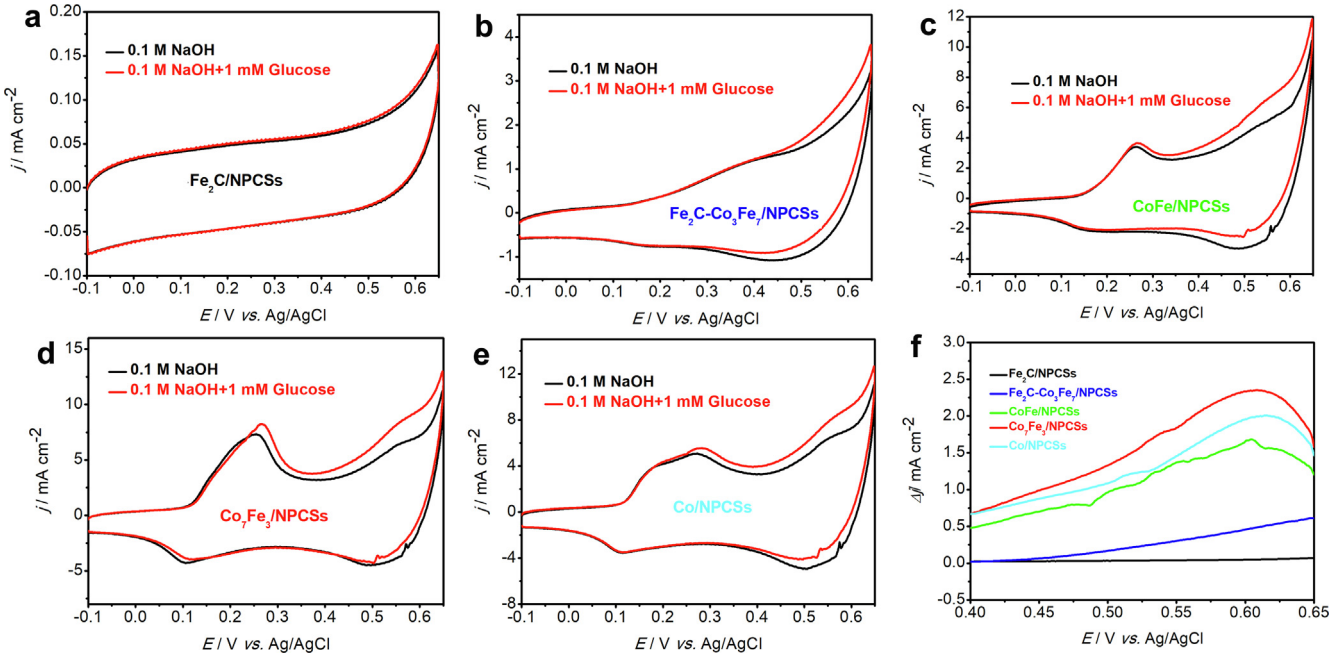

Fig. 5. CV plots of the (a) Fe_2C/NPCSs/Nafion/GCE, (b) Fe_2C-Co_3Fe_7/NPCSs/Nafion/GCE, (c) CoFe/NPCSs/Nafion/GCE, (d) Co_7Fe_3/NPCSs/Nafion/GCE, and (e) Co/NPCSs /Nafion/GCE measured in a 0.1 M NaOH solution prepared without (black lines) and with (red lines) 1.0 mM glucose (scan rate: 50 mV s^{-1}). (f) The corresponding Δj responses of the different catalyst-modified GCEs toward glucose oxidation in the potential range of +0.40 to +0.65 V *vs.* Ag/AgCl. (For interpretation of the references to colour in this figure legend, the reader is referred to the web version of this article.)

added to the 0.1 M NaOH solution, in the potential range of E > +0.45 V *vs.* Ag/AgCl, the Δj values of glucose electro-oxidation increase gradually. The electrochemical oxidation of glucose corresponds to the formation of Co^{4+} ions, which proves that the high valence state Co^{4+} ions act as active sites for glucose oxidation. The CV curves of the CoFe/NPCSs/Nafion/GCE (Fig. 5c), Co_7Fe_3/NPCSs/Nafion/GCE (Fig. 5d), and Co/NPCSs/Nafion/GCE (Fig. 5e) reveal a similar trend. For instance, the irreversible redox pair of Co^{2+}/Co^{3+} appears to be located in the potential region of +0.10 to +0.40 V *vs.* Ag/AgCl. When the working potentials are more positive than +0.40 V *vs.* Ag/AgCl, obvious oxidation peaks appeared at +0.55 V *vs.* Ag/AgCl. In particular, the Δj values toward glucose electro-oxidation appeared once the potential values were larger than +0.25 V *vs.* Ag/AgCl. Even though the CV curve shapes of the CoFe/NPCSs/Nafion/GCE, Co_7Fe_3/NPCSs/Nafion/GCE, and Co/NPCSs/Nafion/GCE are similar, their j values are very different. By comparing the glucose oxidation catalysis activities of the different control samples, the Δj values of glucose oxidation between +0.40 and +0.65 V *vs.* Ag/AgCl are calculated and shown in Fig. 5f. It is clear that in the as-selected potential range of +0.40 to +0.65 *vs.* Ag/AgCl, the Δj values increase by the order of Fe_2C/NPCSs/Nafion/GCE < Fe_2C-Co_3Fe_7/NPCSs/Nafion/GCE < CoFe/NPCSs/Nafion/GCE < Co/NPCSs/Nafion/GCE < Co_7Fe_3/NPCSs/Nafion/GCE. THE Co_7Fe_3/NPCSs exhibit the best catalysis activity toward glucose oxidation. On the other hand, a potential value of +0.60 V *vs.* Ag/AgCl is the optimal glucose oxidation potential for the CoFe/NPCSs/Nafion/GCE, Co_7Fe_3/NPCSs/Nafion/GCE, and Co/NPCSs/Nafion/GCE.

Fig. 6a shows the Nyquist plots obtained by electrochemical impedance spectroscopy (EIS) for the various Co-based control samples. It is clear that in the high frequency range, semicircles are not observed for any of the control samples. This result proves that embedding alloy nanoparticles into the graphitic carbon nanosheets indeed enhances the electron conductivity of each hybrid catalyst. The EIS tests show that the conductivity is not the primary factor leading to the differences in the catalysis activities of the various control catalysts. The double-layer capacitances (C_{dl}) of the four control samples were extracted by plotting the $\Delta j_{at\ 0.55\ V}/2$ values [$\Delta j_{at\ 0.55\ V}/2 = (j_a - j_c)/2$] against the CV scan rates (Fig. 6b). The j_a and j_c values are the corresponding oxidation and reduction j values recorded at +0.55 V *vs.* Ag/AgCl (as shown in Fig. S6), respectively. Fig. 6b shows that the C_{dl} values increase by the order of 10.67 mF cm^{-2} (Fe_2C-Co_3Fe_7/NPCSs) < 48.95 mF cm^{-2} (CoFe/NPCSs) < 54.71 mF cm^{-2} (Co/NPCSs) < 69.63 mF cm^{-2} (Co_7Fe_3/NPCSs). It is well known that the C_{dl} values are directly proportional to the electrochemically active surface areas, and thus, the electrochemically active surface areas also increase by the order of Fe_2C-Co_3Fe_7/NPCSs < CoFe/NPCSs < Co/NPCSs < Co_7Fe_3/NPCSs. Finally, Fig. 6c compares the CV curves of the Fe_2C-Co_3Fe_7/NPCSs/Nafion/GCE, CoFe/NPCSs/Nafion/GCE, Co_7Fe_3/NPCSs/Nafion/GCE and Co/NPCSs/Nafion/GCE measured in a 0.1 M NaOH solution prepared without glucose. It is clear that in the high potential range (E > +0.45 V *vs.* Ag/AgCl), the j values recorded in the positive scan increase by the order of Fe_2C-Co_3Fe_7/NPCSs/Nafion/GCE < CoFe/NPCSs/Nafion/GCE < Co/NPCSs/Nafion/GCE < Co_7Fe_3/NPCSs/Nafion/GCE. In fact, in the high potential range of + 0.45 to + 0.65 V *vs.* Ag/AgCl, the oxidation j values correspond to the formation of high valence state Co^{4+} ions. After the electrochemical polarization, the amount of Co^{4+} active sites formed along the control catalysts' surfaces increased by the order of Fe_2C-Co_3Fe_7/NPCSs < CoFe/NPCSs < Co/NPCSs < Co_7Fe_3/NPCSs.

Combining the abovementioned structural, chemical and electrochemical characterization results, we have determined why the glucose oxidation performances of the Co_7Fe_3/NPCSs have improved significantly. As shown in Figs. 2a-f, S5, 3b and 6a, the morphologies, particle sizes, BET surface areas and electron conductivities are similar for all the control samples. Therefore, these properties are not the main factors leading to the large differences in the glucose oxidation activities. The large differences in the glucose oxidation activities of the various control catalysts containing different Co amounts are mainly attributed to the different surface chemical compositions of the control catalysts. The Fe_2C/NPCSs

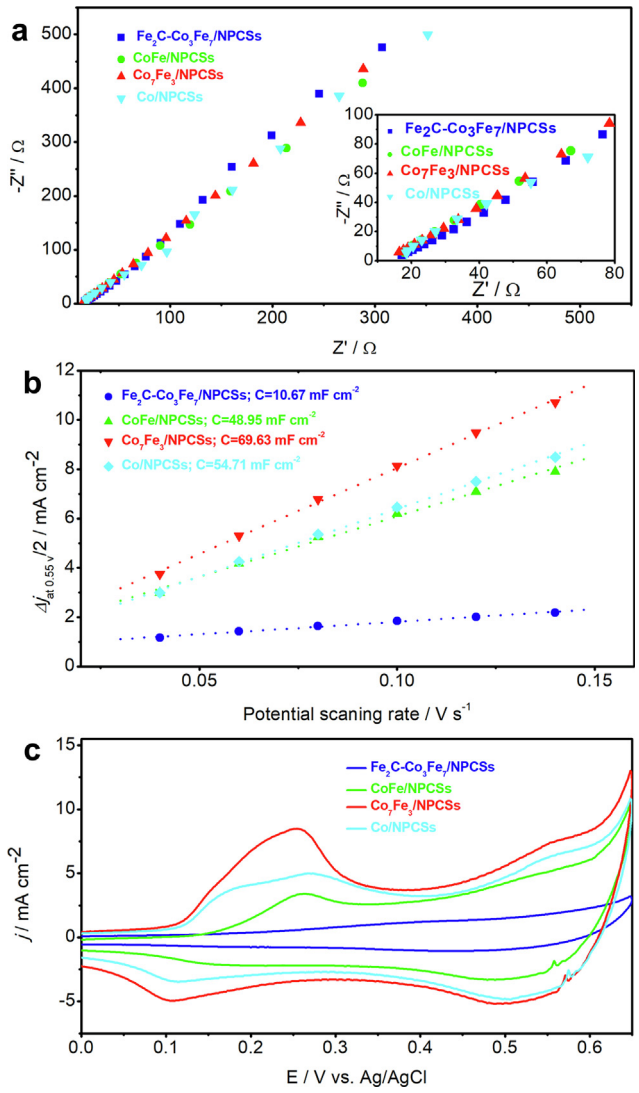

Fig. 6. (a) Nyquist plots obtained by EIS for the Fe_2C-Co_3Fe_7/NPCSs/Nafion/GCE, CoFe/NPCSs/Nafion/GCE, Co_7Fe_3/NPCSs/Nafion/GCE, and Co/NPCSs /Nafion/GCE. Inset shows the magnified images in the high frequency region. (b) The capacitive current responses recorded at +0.55 V *vs.* Ag/AgCl ($\Delta j_{at\ +0.55\ V\ vs.\ Ag/AgC}$) as a function of the scan rates for the different control samples. (c) A comparison of the CV plots of the Fe_2C-Co_3Fe_7/NPCSs/Nafion/GCE, CoFe/NPCSs/Nafion/GCE, Co_7Fe_3/NPCSs/Nafion/GCE, and Co/NPCSs/Nafion/GCE measured in a 0.1 M NaOH solution with a scan rate of 50 mV s^{-1}.

without Co have an inferior glucose oxidation activity compared to the other catalysts, demonstrating that the active sites for glucose oxidation are Co-based species. Because the Fe_2C-Co_3Fe_7/NPCSs, CoFe/NPCSs and Co_7Fe_3/NPCSs catalysts contain both Co and Fe elements, their C_{dl} values (Fig. 6b) and oxidation j values recorded from +0.45 to +0.65 V *vs.* Ag/AgCl in the positive scan of the CV curves increase by the order of Fe_2C-Co_3Fe_7/NPCSs < CoFe/NPCSs < Co_7Fe_3/NPCSs (Fig. 6c). The experimental results indicate that the many Co atoms in the Co_7Fe_3/NPCSs indeed causes more Co^{4+} active sites to form along the surfaces during the polarization process, which results in Co_7Fe_3/NPCSs having a larger electrochemically active surface area and better glucose oxidation ability than the Fe_2C-Co_3Fe_7/NPCSs and CoFe/NPCSs. Finally, although the Co/NPCSs have a higher Co content than the Co_7Fe_3/NPCSs, the C_{dl} value (Fig. 6b) and oxidation j values recorded from +0.45 to +0.65 V *vs.* Ag/AgCl in the positive scan (Fig. 6c) for the Co/NPCSs are lower than those of the Co_7Fe_3/NPCSs. This reveals that the Co_7Fe_3/NPCSs catalyst contains more Co^{4+} active sites along the surfaces after the polarization process, which results in the Co_7Fe_3/NPCSs catalyst having a larger electrochemically active surface area than the Co/NPCSs. Therefore, the Co_7Fe_3/NPCSs also have a better catalysis activity than the Co/NPCSs toward glucose oxidation. A small number of Fe atoms in the Co_7Fe_3 alloy can cause more Co^{4+} active sites to form along the catalysts' surfaces, which is similar to conclusions reported previously in the literature [32]. The HRTEM image (shown in Fig. S7) shows that after carrying out the electrochemical polarization, thin shell layers (with thicknesses of ~5 nm) can be clearly observed surrounding the surfaces of all the Co_7Fe_3 nanoparticles. This phenomenon proves that metallic oxide layers with high metal valences have indeed formed, which is similar to conclusions reported previously in the literature [28].

On the other hand, to determine the effect of pore effect of the plant-tissue-based Co_7Fe_3/NPCSs, we have also synthesized a Co_7Fe_3/NC control sample by utilizing a mixed precursor containing 0.9 mmol $Fe(AC)_2$, 2.1 mmol $Co(AC)_2$, 0.36 mmol CN_2H_2 and 2.9 mmol $C_{12}O_{11}H_{22}$. As shown in the SEM image (Fig. S8a), the Co_7Fe_3/NC consists of a vast bulk material with poor porosity. The TEM image ((Fig. S8b) exhibits that the surfaces of the Co_7Fe_3/NC contain few porous structures, and the alloy nanoparticles are thoroughly embedded in the carbon matrices. As shown in Fig. S9a, the CV curve of the Co_7Fe_3/NC/Nafion/GCE measured in the 0.1 M NaOH solution without glucose is much weaker than that of the Co_7Fe_3/NPCSs/Nafion/GCE. By adding a 1.0 mM glucose solution to a 0.1 M NaOH solution, the Co_7Fe_3/NC/Nafion/GCE also exhibits much smaller Δj values than the Co_7Fe_3/NPCSs/Nafion/GCE (Fig. S9b), indicating the improved catalysis ability of the Co_7Fe_3/NPCSs toward glucose oxidation compared with the Co_7Fe_3/NC. This control experiment obviously proves that the perfect porosity of the Co_7Fe_3/NPCSs indeed enhances the glucose catalytic activity.

From the abovementioned discussions, the superior catalysis ability of the Co_7Fe_3/NPCSs toward glucose oxidation is mainly attributed to the following factors: (1) The superior electron conductivity of the Co_7Fe_3/NPCSs enhances the electron transfer rate of the electrochemical reactions. (2) The hierarchical porous channels derived from the plant tissues and the releases of H_2O/CO_2 gases in the pyrolysis process can promote mass transport during the electrochemical reaction. (3) The abundant meso/macropores afforded the catalyst with a large BET surface area and vast carbon edges/defects, improving the dispersion of the ultrafine alloy nanoparticles and increasing the number of active sites for glucose oxidation catalysis. (4) Doping small amount of Fe atoms into the Co nanoparticles can cause more high-valence state Co^{4+} active sites to form along the catalyst surfaces during the electrochemical polarization processes.

3.3. Amperometric performances of the different catalyst-modified GCEs toward glucose detection

We further measured the glucose sensor performances of the Fe_2C-Co_3Fe_7/NPCSs/Nafion/GCE, CoFe/NPCSs/Nafion/GCE, Co_7Fe_3/NPCSs/Nafion/GCE and Co/NPCSs/Nafion/GCE at the optimal potential of + 0.60 V *vs.* Ag/AgCl by utilizing a chronoamperometry technique. The amperometric responses for successive addition of glucose at + 0.60 V *vs.* Ag/AgCl were measured and are shown in Figs. 7a and S9. The response times (*i.e., the* times required to reach 95% of the steady-state j values) increase by the order of Fe_2C-Co_3Fe_7/NPCSs/Nafion/GCE (4.0 s) < CoFe/NPCSs/Nafion/GCE (3.5 s) < Co/NPCSs/Nafion/GCE (2.8 s) < Co_7Fe_3/NPCSs/Nafion/GCE (2.2 s), demonstrating that Co_7Fe_3/NPCSs/Nafion/GCE has the shortest response time (Figs. 7b and S10). The calibration curves of the four control electrodes were plotted and can be divided into two linear ranges. In the low concentration ranges (Figs. 7c and S11), the detection limit values (S/N = 3) of the Fe_2C-Co_3Fe_7/NPCSs/Nafion/

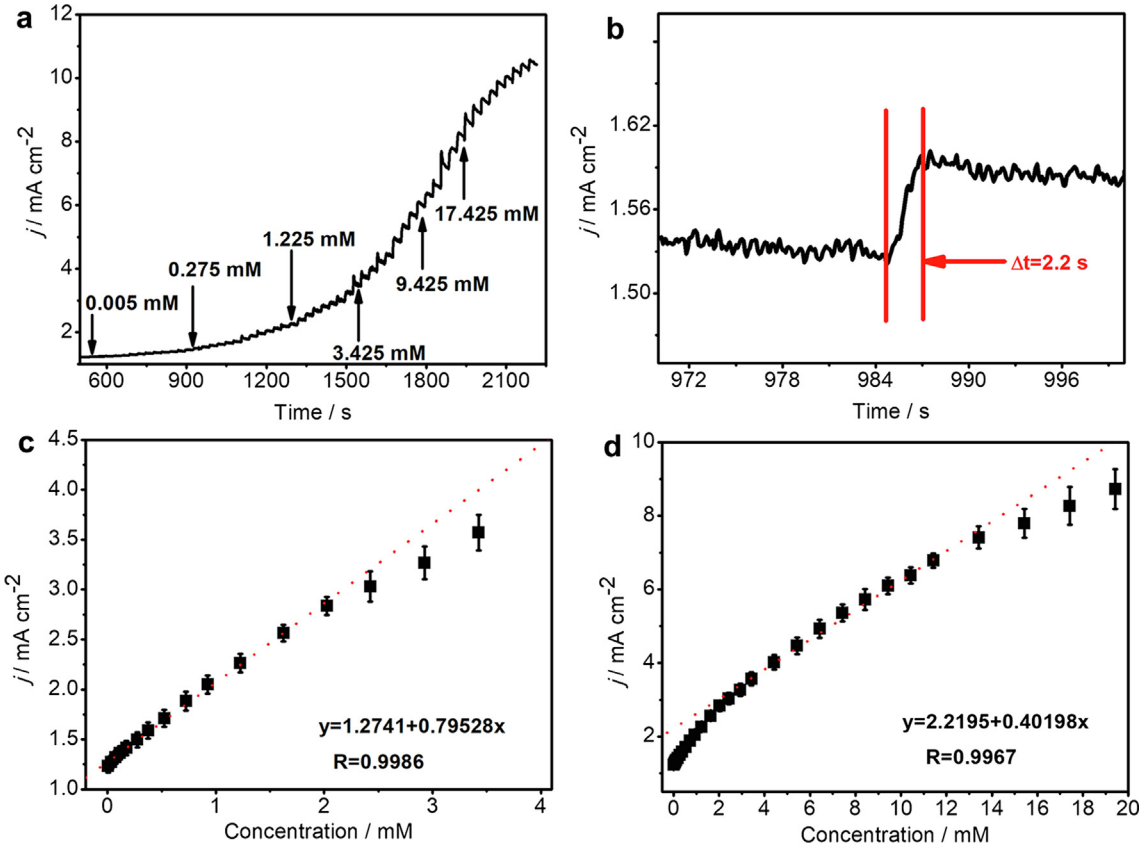

Fig. 7. (a) The amperometric *j–t* curve recorded with the successive addition of glucose into 0.1 M NaOH measured at +0.60 V *vs.* Ag/AgCl, (b) the response time toward glucose oxidation detection, (c) calibration plot in the low glucose concentration range and (d) calibration plot in the high glucose concentration range for the Co_7Fe_3/NPCSs/Nafion/GCE. Three replicate experiments were performed to investigate the calibration plots.

GCE, CoFe/NPCSs/Nafion/GCE, Co_7Fe_3/NPCSs/Nafion/GCE and Co/NPCSs/Nafion/GCE were determined to be 5.0 μM, 5.0 μM, 1.0 μM and 1.0 μM, respectively. The Co_7Fe_3/NPCSs/Nafion/GCE has the lowest detection limit of the other electrodes. The linear low-concentration ranges are 0.005–1.40 mM, 0.005–1.55 mM, 0.001–2.20 mM and 0.001–1.80 mM for the Fe_2C-Co_3Fe_7/NPCSs/Nafion/GCE, CoFe/NPCSs/Nafion/GCE, Co_7Fe_3/NPCSs/Nafion/GCE and Co/NPCSs/Nafion/GCE, respectively. The corresponding sensitivity values calculated for the low-concentration ranges are 272.32 μA mM^{-1} cm^{-2}, 655.10 μA mM^{-1} cm^{-2}, 795.28 μA mM^{-1} cm^{-2}, and 669.58 μA mM^{-1} cm^{-2} for the Fe_2C-Co_3Fe_7/NPCSs/Nafion/GCE, CoFe/NPCSs/Nafion/GCE, Co_7Fe_3/NPCSs/Nafion/GCE, and Co/NPCSs/Nafion/GCE, respectively. In the high glucose concentration ranges (Figs. 7d and S12), the linear ranges and sensitivities are 1.40 to 7.00 mM and 114.73 μA cm^{-2} mM^{-1} (for the Fe_2C-Co_3Fe_7/NPCSs/Nafion/GCE), 1.55 to 8.00 mM and 306.99 μA cm^{-2} mM^{-1} (for the CoFe/NPCSs/Nafion/GCE), 2.20 to 14.00 mM and 401.98 μA cm^{-2} mM^{-1} (for the Co_7Fe_3/NPCSs/Nafion/GCE), and 1.80 to 11.60 mM and 359.45 μA cm^{-2} mM^{-1} (for the Co/NPCSs/Nafion/GCE), respectively. It is obvious that whether in the low or high glucose concentration ranges, Co_7Fe_3/NPCSs/Nafion/GCE exhibits the best glucose detection parameters, including the lowest detection limit, widest linear range, and largest detection sensitivity. As shown in Table S1, compared with the other previously reported Co-based glucose sensors, including Co_3O_4 nanoparticles [37], graphene–cobalt oxide [38], CuCo–CFs [2], Co_4N-NSs [12], $Co_2N_{0.67}$ NSs [39], Co_3N NW [40], CoP NA [41] and CoSe–rGO [42], the Co_7Fe_3/NPCSs catalyst prepared in this work has much wider linear concentration range for glucose detection. Meanwhile, the Co_7Fe_3/NPCSs catalyst developed in this work also has a shorter response time than most of the selected Co-based glucose sensors.

3.4. Interference analysis

Due to the complex compositions of blood, a challenge in glucose detection is eliminating the influences of various interfering reagents. Fig. 8a exhibits the CV curves of the Co_7Fe_3/NPCSs in a 0.1 M NaOH solution containing 1.0 mM glucose prepared with (red line) and without (black line) 0.15 M NaCl. It is obvious that the Co_7Fe_3/NPCSs display an excellent anti-interference capability toward Cl^-. We further investigated the anti-interference ability of the Co_7Fe_3/NPCSs toward other interfering reagents (AA, DA, LA, GA, and UA) (Fig. 8b). One can see that the Co_7Fe_3/NPCSs produce negligible responses by adding 0.1 mM interfering reagents to the 0.1 M NaOH solution containing 1.0 mM glucose. The above-mentioned test results indicate the perfect anti-interference ability of the Co_7Fe_3/NPCSs toward other coexisting electroactive species during glucose detection.

3.5. Reproducibility and stability

We also determined the reproducibility of the ability of Co_7Fe_3/NPCSs to detect glucose oxidation by comparing the current responses of 6 different modified electrodes toward 0.15 mM glucose (as shown in Fig. 8c). Three replicate experiments were performed for each modified electrode, and the amperometric response for each electrode is the average value of the three replicates. It is clear that the amperometric responses of the 6 different Co_7Fe_3/NPCSs/Nafion/GCEs toward 0.15 mM glucose reveal the superior reproducibility of the electrodes with a relative standard deviation (R.S.D.) of 3.74%. Finally, Fig. 8d exhibits the relationships between the current percentages and storage time for one of the Co_7Fe_3/NPCSs/Nafion/GCEs. Three replicate experiments were

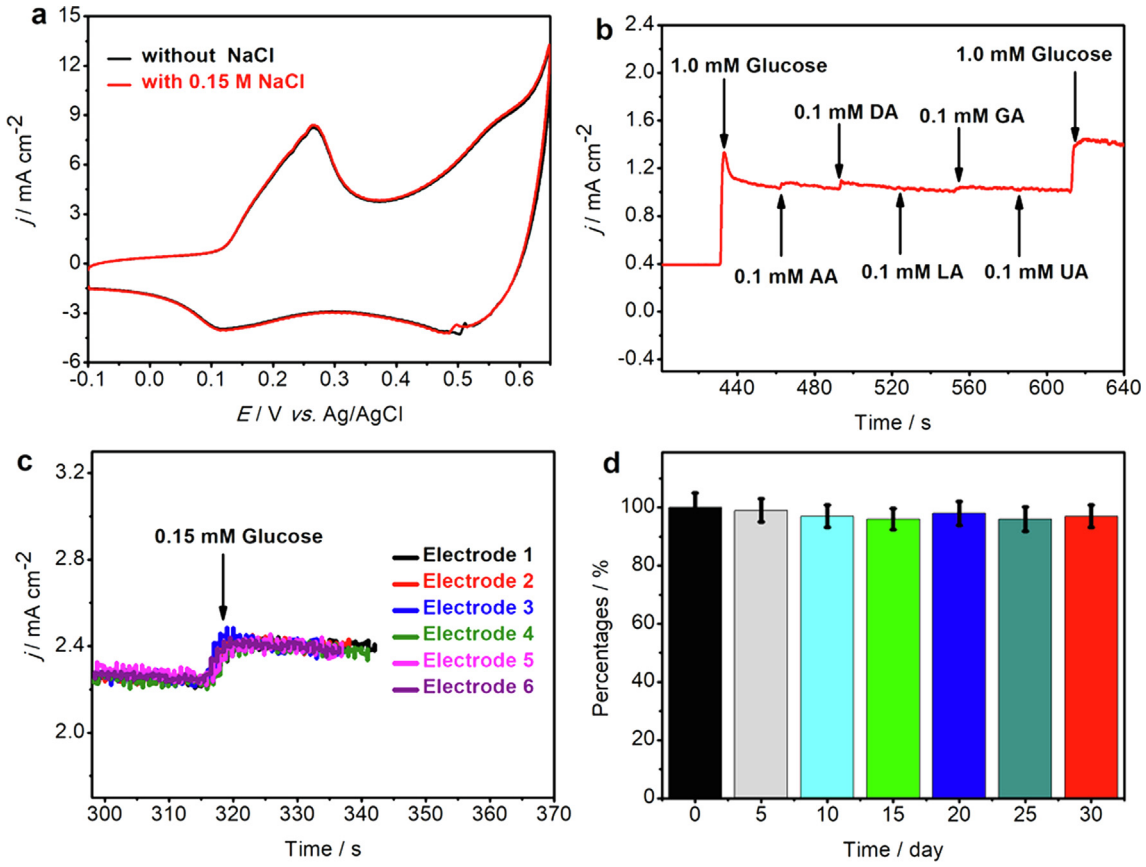

Fig. 8. (a) CV curves of the Co_7Fe_3/NPCSs/Nafion/GCE measured in a 0.1 M NaOH solution containing 1.0 mM glucose prepared without (black line) and with (red line) 0.15 M NaCl (scan rate: 50 mV s^{-1}). (b) The amperometric *j–t* curve of the Co_7Fe_3/NPCSs/Nafion/GCE measured with the successive addition of 1.0 mM glucose, 0.1 mM interference compounds (AA, DA, LA, GA, and UA), and 1.0 mM glucose at + 0.6 V *vs.* Ag/AgCl. (c) The amperometric responses of 6 different Co_7Fe_3/NPCSs/Nafion/GCEs toward 0.15 mM glucose at + 0.6 V *vs.* Ag/AgCl. (d) The stability test of the same Co_7Fe_3/NPCSs/Nafion/GCE toward glucose detection measured every five days for one month. (For interpretation of the references to colour in this figure legend, the reader is referred to the web version of this article.)

performed for each test; the current value was the average value of the three replicates. One can see that the Co_7Fe_3/NPCSs/Nafion/GCE maintains at least 96.5% of the initial current value after one month, demonstrating an excellent long-term stability.

3.6. Real sample analysis

Finally, we explored the feasibility of detecting glucose in human serum samples by using the Co_7Fe_3/NPCSs/Nafion/GCE. As shown in Table S2, the corresponding detection results are satisfying, and all the detection results agree with those measured by utilizing the glucose biosensor used by a local hospital (where each human serum sample was tested four times). The corresponding detection results indicate that the glucose detection ability of our Co_7Fe_3/NPCSs/Nafion/GCE is not only appropriate for testing standard glucose samples but also suitable for testing real human serum samples.

4. Conclusion

In summary, we have successfully synthesized ultrafine Co_7Fe_3 alloy nanoparticles embedded in nitrogen-doped porous carbon nanosheets (denoted as Co_7Fe_3/NPCSs), as reported in this paper. The structural characterization results indicated that large amounts of *meso*/macroporous channels and carbon edges/defects were uniformly dispersed on the Co_7Fe_3/NPCSs, which led to a large BET surface area. Due to the nanoconfined effect of the mesopores and carbon edges/defects, the ultrafine Co_7Fe_3 alloy nanoparticles were uniformly dispersed along the surfaces of the Co_7Fe_3/NPCSs. When utilized for glucose oxidation catalysis and detection, the optimal Co_7Fe_3/NPCSs catalyst exhibited larger glucose catalysis currents, a faster response time, a higher detection sensitivity and a wider linear range than the other control samples (Fe_2C/NPCSs, Fe_2C-Co_3Fe_7/NPCSs, CoFe/NPCSs and Co/NPCSs). Especially, the Co_7Fe_3/NPCSs catalyst prepared in this work has much wider linear concentration range for glucose detection (0.001 to 14.00 mM) compared with the other previously reported Co-based glucose sensors, including Co_3O_4 nanoparticles (0.005–0.80 mM) [37], Co_4N-NSs (0.60 to 10.00 mM) [12], $Co_2N_{0.67}$ NSs (0.01–8.00 mM) [39], and CoSe–rGO (up to 10.00 mM) [42]. Our optimal Co_7Fe_3/NPCSs catalyst also displays a shorter response time and a wider linear range than the other Co-based glucose sensors reported previously. Furthermore, the Co_7Fe_3/NPCSs also display a perfect selectivity and stability for glucose detection. The Co_7Fe_3/NPCSs also exhibit a satisfying efficiency for glucose detection in human serum samples. The excellent glucose sensor activity of the optimal Co_7Fe_3/NPCSs can be attributed to the synergistic effect of excellent electron conductivity, perfect porosity and abundant Co^{4+} active sites. Finally, our low-cost synthetic strategy can advance research in designing three-dimensional hierarchical *meso*/macroporous noble-metal-free catalysts without using any tedious steps or templates.

Acknowledgement

The authors gratefully acknowledge the supports from the scientific research start-up fund from Kunming University of Science and Technology of introducing talents (130214119417) and the

analysis and testing fund from Kunming University of Science and Technology (2018T20170019). We also thank Anaclet Nsabimana for his help in checking the English.

Appendix A. Supplementary material

Supplementary data to this article can be found online at https://doi.org/10.1016/j.jcis.2019.07.099.

References

[1] L. Özcan, Y. Şahin, H. Türk, Non-enzymatic glucose biosensor based on overoxidized polypyrrole nanofiber electrode modified with cobalt (II) phthalocyanine tetrasulfonate, Biosens. Bioelectron. 24 (2008) 512–517.
[2] M. Li, L. Liu, Y. Xiong, X. Liu, A. Nsabimana, X. Bo, L. Guo, Bimetallic MCo (M = Cu, Fe, Ni, and Mn) nanoparticles doped-carbon nanofibers synthetized by electrospinning for nonenzymatic glucose detection, Sens. Actuat., B 207 (2015) 614–622.
[3] K.E. Hellström, I. Hellström, Cellular immunity against tumor antigens, Adv. Cancer Res. 12 (1969) 167–223.
[4] M. Xu, Y. Song, Y. Ye, C. Gong, Y. Shen, L. Wang, L. Wang, A novel flexible electrochemical glucose sensor based on gold nanoparticles/polyaniline arrays/carbon cloth electrode, Sens. Actuat., B 252 (2017) 1187–1193.
[5] L. Wang, Y. Zhang, J. Yu, J. He, H. Yang, Y. Ye, Y. Song, A green and simple strategy to prepare graphene foam-like three-dimensional porous carbon/Ni nanoparticles for glucose sensing, Sens. Actuat., B 239 (2017) 172–179.
[6] C. Chen, R. Ran, Z. Yang, R. Lv, W. Shen, F. Kang, Z.-H. Huang, An efficient flexible electrochemical glucose sensor based on carbon nanotubes/carbonized silk fabrics decorated with Pt microspheres, Sens. Actuat., B 256 (2018) 63–70.
[7] M. Chi, Y. Zhu, L. Jing, C. Wang, X. Lu, Fabrication of ternary MoS_2-polypyrrole-Pd nanotubes as peroxidase mimics with a synergistic effect and their sensitive colorimetric detection of l-cysteine, Anal. Chem. Acta 1035 (2018) 146–153.
[8] H. Yang, Z. Wang, C. Li, C. Xu, Nanoporous PdCu alloy as an excellent electrochemical sensor for H_2O_2 and glucose detection, J. Colloid Interf. Sci. 491 (2017) 321–328.
[9] M. Li, X. Bo, Y. Zhang, C. Han, L. Guo, One-pot ionic liquid-assisted synthesis of highly dispersed PtPd nanoparticles/reduced graphene oxide composites for nonenzymatic glucose detection, Biosens. Bioelectron. 56 (2014) 223–230.
[10] S. Nantaphol, T. Watanabe, N. Nomura, W. Siangproh, O. Chailapakul, Y. Einaga, Bimetallic Pt–Au nanocatalysts electrochemically deposited on boron-doped diamond electrodes for nonenzymatic glucose detection, Biosens. Bioelectron. 98 (2017) 76–82.
[11] M. Li, X. Bo, Z. Mu, Y. Zhang, L. Guo, Electrodeposition of nickel oxide and platinum nanoparticles on electrochemically reduced graphene oxide film as a nonenzymatic glucose sensor, Sens. Actuat., B 192 (2014) 261–268.
[12] T. Liu, M. Li, L. Guo, Designing and facilely synthesizing a series of cobalt nitride (Co_4N) nanocatalysts as non-enzymatic glucose sensors: a comparative study toward the influences of material structures on electrocatalytic activities, Talanta 181 (2018) 154–164.
[13] Q. Guo, M. Zhang, S. Liu, G. Zhou, X. Li, H. Hou, L. Wang, Facile synthesis of Ni $(OH)_2$ nanoplates on nitrogen-doped carbon foam for nonenzymatic glucose sensors, Anal. Methods 8 (2016) 8227–8233.
[14] M. Li, C. Han, Y. Zhang, X. Bo, L. Guo, Facile synthesis of ultrafine Co_3O_4 nanocrystals embedded carbon matrices with specific skeletal structures as efficient non-enzymatic glucose sensors, Anal. Chem. Acta 861 (2015) 25–35.
[15] M. Li, Z. Zhao, X. Liu, Y. Xiong, C. Han, Y. Zhang, X. Bo, L. Guo, Novel bamboo leaf shaped CuO nanorod@hollow carbon fibers derived from plant biomass for efficient and nonenzymatic glucose detection, Analyst 140 (2015) 6412–6420.
[16] Y. He, X. Li, X. Xu, J. Pan, X. Niu, A cobalt-based polyoxometalate nanozyme with high peroxidase-mimicking activity at neutral pH for one-pot colorimetric analysis of glucose, J. Mater. Chem. B 6 (2018) 5750–5755.
[17] S.-J. Li, L.-L. Hou, B.-Q. Yuan, M.-Z. Chang, Y. Ma, J.-M. Du, Enzyme-free glucose sensor using a glassy carbon electrode modified with reduced graphene oxide decorated with mixed copper and cobalt oxides, Microchim. Acta 183 (2016) 1813–1821.
[18] H. Zhang, S. Liu, A combined self-assembly and calcination method for preparation of nanoparticles-assembled cobalt oxide nanosheets using graphene oxide as template and their application for non-enzymatic glucose biosensing, J. Colloid Interf. Sci. 485 (2017) 159–166.
[19] R. Madhu, V. Veeramani, S.-M. Chen, A. Manikandan, A.-Y. Lo, Y.-L. Chueh, Honeycomb-like porous carbon–cobalt oxide nanocomposite for high-performance enzymeless glucose sensor and supercapacitor applications, ACS Appl. Mater. Inter. 7 (2015) 15812–15820.
[20] L. Wang, Q. Teng, X. Sun, Y. Chen, Y. Wang, H. Wang, Y. Zhang, Facile synthesis of metal-organic frameworks/ordered mesoporous carbon composites with enhanced electrocatalytic ability for hydrazine, J. Colloid Interf. Sci. 512 (2018) 127–133.
[21] M. Li, X. Liu, Y. Xiong, X. Bo, Y. Zhang, C. Han, L. Guo, Facile synthesis of various highly dispersive CoP nanocrystal embedded carbon matrices as efficient electrocatalysts for the hydrogen evolution reaction, J. Mater. Chem. A 3 (2015) 4255–4265.
[22] T. Meng, L. Wang, H. Jia, T. Gong, Y. Feng, R. Li, H. Wang, Y. Zhang, Facile synthesis of platinum-embedded zirconia/porous carbons tri-component nanohybrids from metal-organic framework and their application for ultra-sensitively detection of methyl parathion, J. Colloid Interf. Sci. 536 (2019) 424–430.
[23] J. Xiao, C. Chen, J. Xi, Y. Xu, F. Xiao, S. Wang, S. Yang, Core–shell Co@Co_3O_4 nanoparticle-embedded bamboo-like nitrogen-doped carbon nanotubes (BNCNTs) as a highly active electrocatalyst for the oxygen reduction reaction, Nanoscale 7 (2015) 7056–7064.
[24] Z. Guo, F. Wang, Y. Xia, J. Li, A.G. Tamirat, Y. Liu, L. Wang, Y. Wang, Y. Xia, In situ encapsulation of core–shell-structured Co@Co_3O_4 into nitrogen-doped carbon polyhedra as a bifunctional catalyst for rechargeable Zn–air batteries, J. Mater. Chem. A 6 (2018) 1443–1453.
[25] Y. Zhao, X. Bo, L. Guo, Highly exposed copper oxide supported on three-dimensional porous reduced graphene oxide for non-enzymatic detection of glucose, Electrochim. Acta 176 (2015) 1272–1279.
[26] X. Kong, Y. Wang, Q. Zhang, T. Zhang, Q. Teng, L. Wang, H. Wang, Y. Zhang, Ex-situ decoration of ordered mesoporous carbon with palladium nanoparticles via polyoxometalates and for sensitive detection of acetaminophen in pharmaceutical products, J. Colloid Interf. Sci. 505 (2017) 615–621.
[27] Q. Teng, Y. Chen, X. Sun, Y. Wang, F. Li, L. Wang, J. Zhao, H. Wang, Y. Zhang, Formation of Fe_2O_3 microboxes/macroporous carbon hybrids from Prussian blue template for electrochemical applications, J. Alloy. Compd. 739 (2018) 425–430.
[28] T. Liu, M. Li, Z. Su, X. Bo, W. Guan, M. Zhou, Monodisperse and tiny $Co_2N_{0.67}$ nanocrystals uniformly embedded over two curving surfaces of hollow carbon microfibers as efficient electrocatalyst for oxygen evolution reaction, ACS Appl. Nano Mater. 1 (2018) 4461–4473.
[29] T. Liu, M. Li, C. Jiao, M. Hassan, X. Bo, M. Zhou, Design and synthesis of integrally structured Ni_3N nanosheets/carbon microfibers/Ni_3N nanosheets for efficient full water splitting catalysis, J. Mater. Chem. A 5 (2017) 9377–9390.
[30] M. Li, Y. Xiong, X. Liu, X. Bo, Y. Zhang, C. Han, L. Guo, Facile synthesis of electrospun MFe_2O_4 (M = Co, Ni, Cu, Mn) spinel nanofibers with excellent electrocatalytic properties for oxygen evolution and hydrogen peroxide reduction, Nanoscale 7 (2015) 8920–8930.
[31] M. Li, T. Liu, X. Bo, M. Zhou, L. Guo, A novel flower-like architecture of FeCo@NC-functionalized ultra-thin carbon nanosheets as a highly efficient 3D bifunctional electrocatalyst for full water splitting, J. Mater. Chem. A 5 (2017) 5413–5425.
[32] T. Liu, M. Li, X. Bo, M. Zhou, Comparison study toward the influence of the second metals doping on the oxygen evolution activity of cobalt nitrides, ACS Sustain. Chem. Eng. 6 (2018) 11457–11465.
[33] C. You, X. Jiang, L. Han, X. Wang, Q. Lin, Y. Hua, C. Wang, X. Liu, S. Liao, Uniform nitrogen and sulphur co-doped hollow carbon nanospheres as efficient metal-free electrocatalysts for oxygen reduction, J. Mater. Chem. A 5 (2017) 1742–1748.
[34] X.D. Guo, X.J. Qiao, Q.G. Ren, X. Wan, W.C. Li, Z.G. Sun, Synthesis and microwave-absorbing properties of Co_3Fe_7@C core–shell nanostructure, Appl. Phys. A 120 (2015) 43–52.
[35] P. Cai, Y. Hong, S. Ci, Z. Wen, In situ integration of CoFe alloy nanoparticles with nitrogen-doped carbon nanotubes as advanced bifunctional cathode catalysts for Zn–air batteries, Nanoscale 8 (2016) 20048–20055.
[36] M. Li, Y. Xiong, X. Liu, C. Han, Y. Zhang, X. Bo, L. Guo, Iron and nitrogen co-doped carbon nanotube@hollow carbon fibers derived from plant biomass as efficient catalysts for the oxygen reduction reaction, J. Mater. Chem. A 3 (2015) 9658–9667.
[37] C. Hou, Q. Xu, L. Yin, X. Hu, Metal–organic framework templated synthesis of Co_3O_4 nanoparticles for direct glucose and H_2O_2 detection, Analyst 137 (2012) 5803–5808.
[38] X. Wang, X. Dong, Y. Wen, C. Li, Q. Xiong, P. Chen, A graphene–cobalt oxide based needle electrode for non-enzymatic glucose detection in micro-droplets, Chem. Commun. 48 (2012) 6490–6492.
[39] T. Liu, M. Li, P. Dong, Y. Zhang, L. Guo, Design and facile synthesis of mesoporous cobalt nitride nanosheets modified by pyrolytic carbon for the nonenzymatic glucose detection, Sens. Actuat., B 255 (2018) 1983–1994.
[40] F. Xie, X. Cao, F. Qu, A.M. Asiri, X. Sun, Cobalt nitride nanowire array as an efficient electrochemical sensor for glucose and H_2O_2 detection, Sens. Actuat., B 255 (2018) 1254–1261.
[41] Y. Liu, X. Cao, R. Kong, G. Du, A.M. Asiri, Q. Lu, X. Sun, Cobalt phosphide nanowire array as an effective electrocatalyst for non-enzymatic glucose sensing, J. Mater. Chem. B 5 (2017) 1901–1904.
[42] M.C.D. Cooray, X. Zhang, Y. Zhang, S.J. Langford, Alan M. Bond, J. Zhang, Cobalt selenide nanoflake decorated reduced graphene oxide nanocomposite for efficient glucose electro-oxidation in alkaline medium, J. Mater. Chem. A 5 (2017) 19289–19296.